Three-dimensional morphological analysis of intracranial aneurysms: a fully automated method for aneurysm sac isolation and quantification

Ignacio Larrabide
Networking Research Center on Bioengineering, Biomaterials and Nanomedicine (CIBER-BBN), Barcelona, Spain and Center for Computational Imaging and Simulation Technologies in Biomedicine (CISTIB), Universitat Pompeu Fabra, Barcelona, Spain

Maria Cruz Villa-Uriol, Rubén Cárdenes, and Jose Maria Pozo
Center for Computational Imaging Simulation Technologies in Biomedicine (CISTIB), Universitat Pompeu Fabra, Barcelona, Spain and Networking Research Center on Bioengineering, Biomaterials and Nanomedicine (CIBER-BBN), Barcelona, Spain

Juan Macho, Luis San Roman, and Jordi Blasco
Department of Vascular Radiology, Hospital Clinic i Provincial de Barcelona, Barcelona, Spain

Elio Vivas
Neuroangiograía Terapéutica J.J.Merland, Hospital General de Catalunya, San Cugat del Valles, Spain

Alberto Marzo and D. Rod Hose
Academic Unit of Medical Physics, Faculty of Medicine and Biomedical Sciences, University of Sheffield, Sheffield, UK

Alejandro F. Frangi
Center for Computational Imaging Simulation Technologies in Biomedicine (CISTIB), Universitat Pompeu Fabra, Barcelona, Spain and Networking Research Center on Bioengineering,

Biomaterials and Nanomedicine (CIBER-BBN), Barcelona,
Spain and Institució Catalana de Recerca i Estudis Avançats (ICREA), Barcelona, Spain

Abstract

Purpose: Morphological descriptors are practical and essential biomarkers for diagnosis and treatment selection for intracranial aneurysm management according to the current guidelines in use. Nevertheless, relatively little work has been dedicated to improve the three-dimensional quantification of aneurysmal morphology, automate the analysis, and hence reduce the inherent intra- and inter-observer variability of manual analysis. In this paper we propose a methodology for the automated isolation and morphological quantification of saccular intracranial aneurysms based on a 3D representation of the vascular anatomy.

Method: This methodology is based on the analysis of the vasculature skeleton's topology and the subsequent application of concepts from deformable cylinders. These are expanded inside the parent vessel to identify different regions and discriminate the aneurysm sac from the parent vessel wall. The method renders as output the surface representation of the isolated aneurysm sac, which can then be quantified automatically. The proposed method provides the means for identifying the aneurysm neck in a deterministic way. The results obtained by the method were assessed in two ways: they were compared to manual measurements obtained by three independent clinicians as normally done during diagnosis and to automated measurements from manually isolated aneurysms by three independent operators, non-clinicians, experts in vascular image analysis. All the measurements were obtained using in-house tools. The results were qualitatively and quantitatively compared for a set of saccular intracranial aneurysms (n=26).

Results: Measurements performed on a synthetic phantom showed that the automated measurements obtained from manually isolated aneurysms where the most accurate. The differences between the measurements obtained by the clinicians and the manually isolated sacs were statistically significant (neck width: $p<0.001$, sac height: $p=0.002$). When comparing clinicians' measurements to automatically isolated sacs, only the differences for neck width were significant (neck width: $p<0.001$, sac height: $p=0.95$). However, the correlation and agreement between the measurements obtained from manually and automatically isolated aneurysms for neck width: $p=0.43$ and sac height: $p=0.95$ where found..

Conclusion: The proposed method allows the automated isolation of intracranial aneurysms, eliminating the inter-observer variability. In average, the computational cost of the automated method (2 min. 36 sec.) was similar to the time required by a manual operator (measurement by

clinicians: 2 min. 51 sec., manual isolation: 2 min. 21 sec.) but eliminating human interaction. The automated measurements are irrespective of the viewing angle, eliminating any bias or difference between observer criteria. Finally, the qualitative assessment of the results showed acceptable agreement between manually and automatically isolated aneurysms.

30 Keywords: intracranial aneurysm quantification, automated isolation, deformable models, skeleton analysis,
31 validation

I. INTRODUCTION

Intracranial aneurysms (IA) are abnormal dilatations of the arteries at the Circle of Willis whose rupture can lead to catastrophic complications such as hemorrhagic stroke [1, 2]. The delineation of the aneurysm neck, a hypothetical curve on the vascular wall which separates the balloon-like structure of the aneurysm from its parent artery (see Figure 3(b)), is important not only for its clinical relevance with respect to the genesis and evolution of the disease [3] but also for its treatment planning [4, 5]. In fact, neck delineation is a challenging topic for medical image analysis and yet an open problem. Nowadays, simple morphological measurements of IA such as neck width, sac height, volume and aspect ratio (AR, defined as the ratio between sac height and neck width) are widely used in the clinical evaluation of IA. These measurements are considered for: a) treatment planning: coil and stent implantation are regularly performed as part of standard clinical practice; b) biomarkers for the risk of rupture: it is yet not standard, but there is growing evidence in literature supporting this hypothesis [6–8]. These measurements are manually obtained by radiologists and clinicians with the subsequent subjectivity and variability upon different observers. The detection and quantification of intracranial aneurysms by the "naked eye" is often unprecise and observer/view point dependant [9]. The automatization of this process should make it more precise by removing observer dependency.

To the date, relatively little work has been devoted to automatize the detection, isolation and quantification process of IA. Arimura et al. [10] developed, and later improved [11], a method to aid clinicians detecting the location of potential aneurysms in Magnetic Resonance Angiography (MRA) images. This elegant technique is based on image processing filters for extracting the skeleton representation of the vasculature to detect aneurysm-like features. Fleming et al. [12] developed an automated method for micro aneurysm detection applied to retinopathy. The authors showed how contrast normalization could improve the ability to distinguish between micro aneurysms and other dots occurring on the retina. Uchiyama et al. [13] developed a methodology for automated realtime detection of aneurysms in MRA maximum intensity projection (MIP) images. In the work of Wong and Chung [4], the authors developed a method for the automated detection of vessel abnormalities and the approximation of post-treatment vessel diameters. Ford et al. [14] proposed a methodology for aneurysm removal, which reconstructed the original vessel lumen (i.e. before the

aneurysm exists). This method was based on tools previously developed by Piccinelli et al. [15] where Voronoi diagrams were used to identify the different regions of the vasculature and splines were used to reconstruct the missing part of the original vessel lumen. Lauric et al. [16] presented a method for aneurysm isolation based on geometrical characteristics and topology of the vasculature. Still, none of these methodologies has been compared or assessed against manual measurements used as ground truth.

Automated aneurysm isolation and morphological quantification have not been proposed and properly assessed in the literature. To isolate and automatically quantify saccular intracranial aneurysms, the detection of the aneurysm neck is mandatory. After identifying the neck and isolating the aneurysm sac, it is possible to automatically determine the most relevant morphological characteristics of the aneurysm.

In this work, a methodology for the automated isolation and quantification of saccular intracranial aneurysms is proposed. From the surface representation of the vascular wall provided by a vascular segmentation, and based on the analysis of the vessel geometry, relevant morphological measurements are extracted. With this in mind, we propose a methodology based on deformable models, topological and geometrical analysis for automatically isolating the aneurysm sac and computing morphological measurements.

II. METHODS

We describe a methodology for the automated isolation and morphological quantification of saccular intracranial aneurysms. The analysis is focused on the vascular region of interest (ROI) nearby the aneurysm, which is provided as a surface. Selection of the vascular ROI is not considered as part of this method. This analysis is performed following three steps: i) skeleton processing, ii) aneurysm neck identification and iii) aneurysm quantification (see Figure 2). The method is generic and could be applied to images acquired from any imaging modality. In the current work, it was tested on 3D Rotational Angiography (3DRA) images, which is considered as the gold standard for imaging the intracranial vascular anatomy [17].

We assure that saccular aneurysms present only one ostium located at the interface with the parent vessel. The aneurysm ostium corresponds with its neck at the vascular wall. The outputs of the automated quantification are quantitative indicators of aneurysm size: neck width, sac height, sac area and sac volume. Fusiform aneurysms were excluded from this

study, due to the difficulties in defining their neck.

A. Vascular geometry extraction

Given the original image, a geometrical representation of the vascular wall S at a ROI nearby the aneurysm was obtained. For this, a medical image segmentation method based on Geodesic Active Regions (GAR) [18] was used. GAR is based on the geometric deformable model within the level set framework. The internal force of the deformable model is defined as the local curvature of the evolving surface, while the external one combines region-based descriptors with gradient ones to drive the evolution of the model towards the vascular boundaries. An extensive validation of this method has been presented in [19].

For the extraction of the ROI embedding the aneurysm by the user, different alternatives exist. The simplest one involves the definition of a cropping box that contains the aneurysm and then trimming the vessels that are intersected by the box. A second option is the use of a vessel cutting tool, which cuts the vessels through a plane perpendicular to the vessel centerline at a selected point in it.

B. Skeleton processing

In order to analyze the topology and shape of the vascular ROI, its skeleton L was extracted and analyzed from the triangulated surface representing the vascular wall S. The skeleton L is defined as the set of connected 3D curves centered in the vessel axis.

Skeleton computation. For the extraction of L from S, a flux driven homotopic thinning algorithm was used [20]. An implementation of this method, in the context of the Insight Toolkit (ITK), was provided by Mellado et al. [5]. From the skeleton computation, a tree like structure was obtained where each branch is a 3D curve $l^i \subset L$. For each point $\mathbf{x} \in L$, an estimation of the vessel diameter was computed as the distance to the closest point on S.

Skeleton labeling. The terminal branches of L were identified. A branch l^i is said to be terminal if it is connected to the rest of the skeleton through only one end. The set of terminal branches is denoted as $T(L)$. Then,

$$T(L) \equiv \{l^i \subset L : l^i \cap F \neq \emptyset\},$$

where F is the set of end points in L. We refer to the "connected end" of $l^i \subset T(L)$ as $\mathbf{x}_c$ and to the "free end" of $l^i \subset T(L)$ as $\mathbf{x}_f \in F$.

After identifying terminal branches, the surface S was used to select branch $l^i \subset T(L)$ pointing into the aneurysm (recalled as aneurysm branch). We denote as $C(S)$ the set of vascular wall boundaries. The aneurysm was located approximately at the center of the vascular ROI, which was sufficiently large to include a portion of the aneurysm's parent vessels. Each boundary $\phi \subset C(S)$ is a closed curve in $\mathbb{R}^3$, which represents a vascular ROI opening (see Figure 3(a)). Each $\phi \subset C(S)$ was then associated to one $l^i \subset T(L)$. For this, the skeleton definition, which indicates that each skeleton point $\mathbf{x}$ is locally equidistant to the surface [21], was considered. This implies that it exists a skeleton terminal at approximately half the diameter of ϕ for any opening $\phi \subset C(S)$. Then, $\forall\ l^i \subset T(L)\ \Rightarrow$

a) it exists a point in l^i whose distance to any point in ϕ is less than the vessel diameter at $\mathbf{x}_f$, for any $\phi \subset C(S)$, or

b) all the points in l^i are at one diameter or more from ϕ, for any $\phi \subset C(S)$.

Considering b), we define the set of all terminals $l^i \subset T(L)$ that cannot be paired with one open boundary of the geometry as $A(L)$. Skeleton branches $l^a \subset A(L)$ were considered potential aneurysm branches (Figure 3(a)). The aneurysm neck identification was then performed based on one $l^a \subset A(L)$. For vascular regions with more than one aneurysm, the identification process can be repeated for each $l^a \subset A(L)$.

C. Aneurysm neck identification

Centerlines computation. To initialize the deformable model used to isolate the aneurysm sac, all the centerlines that intersect $l^a \subset A(L)$ were identified. We define $\mathbf{x}_c(l^a)$ as the point connecting l^a to the rest of the skeleton. By centerline, we mean a line over L connecting two branches $l^i, l^j \subset L$ at distance r over L from $\mathbf{x}_c(l^a)$. We denote this centerline as $c^{i,j} = c(l^i, l^j)$. Then, we define:

$$R(L, l^a, r)\ \equiv\ \{l^i \subset L : l^i \text{ is at distance } \leq r \text{ over } L \text{ from } \mathbf{x}_c(l^a)\},$$

where r is the search distance from $\mathbf{x}_c(l^a)$.

To completely isolate the aneurysm from the surrounding vasculature, the centerline has to start and finish at a healthy region of the vasculature. Therefore, it was required to identify healthy regions of the vasculature immediately upstream and downstream from the aneurysm to estimate r. In the case of saccular aneurysms, which are most frequently found in the cerebral vasculature, a criteria of 5 diameters over L starting from $\mathbf{x}_c(l^a)$ of the aneurysm's parent vessel has sufficed to reach the healthy region of the vessel for the cases included in this study. For bifurcation aneurysms, many different centerlines could exist (see Figure 3(a)). We then compute the path over L for each pair $l^i, l^j \in R(L, l^a, r)$.

Simplex deformable model. To isolate the aneurysm sac from the rest of the vasculature, 2-simplex deformable models were used. A 2-simplex is the dual representation of a triangular mesh (Figure 1(a)). Each deformable model was initialized as a curved cylinder with its axis aligned to the pre-computed centerlines $c^{i,j}$ and with its longitudinal center at $\mathbf{x}_c \in l^a$. This cylinder was considered as a set of rings V, each one having a center of mass $\mathbf{c}_V$. For each ring V a set of points arranged in a circular fashion perpendicular to the centerline, was initialized. A mesh $\mathbf{M}$ representing the 2-simplex deformable model was created using a regular grid of points $\mathbf{x}_i \in \mathbb{R}^3$, which spans a cylindrical surface. This mesh connects the rings (5 diameters in each direction from $\mathbf{x}_c(l^a)$ for a total length of 10 diameters) and sweeps around the centerline (2π). Different mesh resolutions can be selected for the simplex mesh. For this study, a mesh of 20 nodes on the longitudinal direction and 20 nodes on the circumferential direction were considered as this mesh resolution was enough to capture the relevant details on the vessel geometry. See Figure 1(b) for a detail on the cylindrical mesh construction.

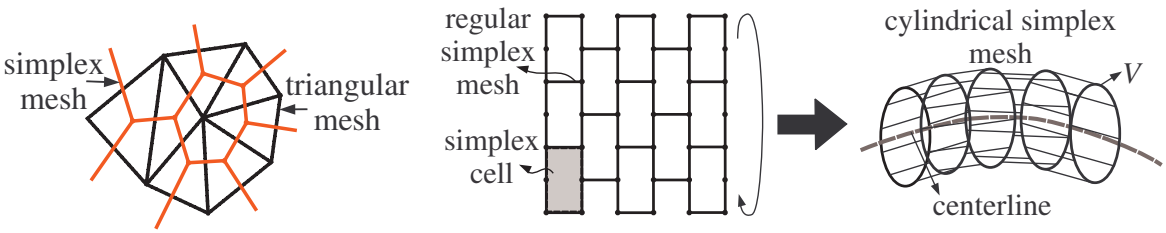

(a) (b)

FIG. 1: (a)A 2-simplex is dual to a triangulated surface. (b) Detail showing the construction of the cylindrical mesh.

After initialization, each model was deformed under the effect of internal and external

forces [22]. For describing the mesh movement, the following Partial Differential Equation (PDE) was considered:

$$\frac{\partial^2 \mathbf{x}_i(t)}{\partial t^2} + \gamma \frac{\partial \mathbf{x}_i(t)}{\partial t} - \mathbf{f}_{int}(\mathbf{x}_i(t)) = \mathbf{f}_{ext}(\mathbf{x}_i(t)). \tag{1}$$

Then, it was discretized as follows using finite differences:

$$\mathbf{x}_i^{t+1} = \mathbf{x}_i^t + (1-\gamma)(\mathbf{x}_i^t - \mathbf{x}_i^{t-1}) + \mathbf{f}_{int}(\mathbf{x}_i^t) + \mathbf{f}_{ext}(\mathbf{x}_i^t), \tag{2}$$

where $\mathbf{f}_{int}(\mathbf{x}_i^t)$ is the internal force acting on $\mathbf{x}_i^t$, $\mathbf{f}_{ext}(\mathbf{x}_i^t)$ is the corresponding external force at the same point and γ represents damping [23]. The index t represents the iteration number, which was omitted in the remainder of the text for simplicity. Internal forces were accounted for as:

$$\mathbf{f}_{int}(\mathbf{x}_i) = \mathbf{f}_s(\mathbf{x}_i) + \mathbf{f}_{exp}(\mathbf{x}_i), \tag{3}$$

where $\mathbf{f}_s$ is the smoothing force, ensuring that the points are homogeneously distributed over the mesh and acts only on the mesh tangential direction; and $\mathbf{f}_{exp}$ is the expanding force ensuring that the vessel wall is reached and acts on the mesh normal direction. The external force $\mathbf{f}_{ext}(\mathbf{x}_i)$ is only active for the points that reached the vessel wall S. These forces are described below.

- Smoothing forces ($\mathbf{f}_s$): The smoothing force [24]

$$\mathbf{f}_s(\mathbf{x}_i) = (\mathbf{x}_i^* - \mathbf{x}_i), \tag{4}$$

  is tangent to the mesh, where $\mathbf{x}_i^*$ corresponds to the position of $\mathbf{x}_i$ ensuring a smooth distribution of the mesh points. Further details on the smoothing forces can be found in the work of Montagnat and Delingette [22].

- Expanding force ($\mathbf{f}_{exp}$): To expand the tubular mesh to reach the vessel wall, a spring model acting along the radial direction of each ring V of the mesh was used. The vessel radius at that position was used as the initial radius of V. We denote the spring rest radius as r_0, which was set to 1.5 times the maximum radius of the vessel covered by the mesh. The magnitude of the expanding force, with a direction normal to the mesh ($\mathbf{n}_i$), can be expressed using the Hooke's law:

$$\|\mathbf{f}_{exp}(\mathbf{x}_i)\| = k(r_0 - \|\mathbf{x}_i - \mathbf{c}_V\|), \tag{5}$$

where k is the stiffness of the spring and was defined as follows:

$$k = E/r_0, \tag{6}$$

being E the Young's elasticity modulus of the spring ($E \sim 0.5N/m^2$ was considered). All the points on the same ring V are maintained at similar distance from the corresponding center of mass $\mathbf{c}_V$ ensuring that the deforming mesh is kept approximately cylindrical. Hence, the mean radius of section $\overline{r}_V$ is given by

$$\overline{r}_V = \frac{1}{n_V} \sum_{k=1}^{n_V} \|\mathbf{x}_k - \mathbf{c}_V\|, \tag{7}$$

where n_V is the number of points in each ring V and is constant for all rings within the mesh. Then, η_i enforces this constraint as follows:

$$\eta_i = \begin{cases} \|\mathbf{x}_k - \mathbf{c}_V\| \leq p\ \overline{r}_V,\ 1; \\ \|\mathbf{x}_k - \mathbf{c}_V\| > p\ \overline{r}_V,\ 0. \end{cases}$$

The value p is the threshold limit for η_i and is a parameter of the model. To determine the value of p, a series of 20 cross sections of arteries for 5 patients (2 internal carotid artery and 2 middle cerebral artery measurements for each patient) were considered. After measuring their maximum and minimum diameters, a 30% difference on average was found between both measurements (min. = 0,2%, max. = 62%, median = 29%). Then, $p = 1.3$ was considered. All parameters have been fixed previous to the validation. No feed-back was used from it to improve the results.

Therefore, $\mathbf{f}_{exp}$ can be written as:

$$\mathbf{f}_{exp}(\mathbf{x}_i) = \mathbf{n}_i \eta_i k(r_0 - \|\mathbf{x}_i - \mathbf{c}_V\|). \tag{8}$$

- External forces ($\mathbf{f}_{ext}$): The mesh expansion was stopped when the deformable model reached the vessel wall. For this, the point to surface distance was computed from each node $\mathbf{x}_i$ to the closest location on S. This force was modeled as being equal in magnitude and in the opposite direction to $\mathbf{f}_{exp}(\mathbf{x}_i)$ for points $\mathbf{x}_i$ over S. Points crossing S were projected back to it, ensuring that the simplex mesh remains inside the vessel at all times. Then, all the points $\mathbf{x}_i \in \mathbf{M}$ are assigned the label $M(\mathbf{x}_i)$ as:

$$M(\mathbf{x}_i) = \begin{cases} 0, & \text{if } \mathbf{x}_i \text{ reached } S; \\ 1, & \text{otherwise.} \end{cases} \tag{9}$$

The initialization and deformation process was repeated for the different centerlines. For each mesh, when internal and external forces were balanced, the mesh movement was negligible, impeding new points from reaching the surface. Then, the deformation process was stopped when, in $n = 20$ consecutive iterations, no new points reached the vessel surface.

D. Aneurysm quantification

Aneurysm sac detachment: For each point $\mathbf{x} \in S$, the closest point $\mathbf{x}_i \in \mathbf{M}$ was identified and the label $M(\mathbf{x}_i)$ was mapped on $\mathbf{x}$. Regions in S where $M(\mathbf{x}) = 1$ were candidates to correspond to the aneurysm sac. The single continuous region presenting $M(\mathbf{x}) = 1$ and closest to the point $\mathbf{x}_c \in l^a$ was identified as the aneurysm sac. For the aneurysm neck, the boundary between the sac and the rest of the vascular wall was considered, which is a non-planar surface. Its average normal, denoted $\mathbf{n}_n$, was also computed. This normal and the neck centroid $\mathbf{x}_c$ define the ostium mean plane.

Morphological quantification: For the automated morphological quantification of the aneurysm from the surface representation of the sac, we define the neck width, the sac height, the area and the volume as follows (see Figure 3(b)):

- *Neck width* w_{neck}: was defined as the maximum distance between two points on the aneurysm neck.
- *Sac height* h_{sac}: the point $\mathbf{x}$ on the sac with the largest projection to the plane defined by $\mathbf{n}_n$ and $\mathbf{x}_c$ was found. Then, h_{sac} was computed as the distance between such point and $\mathbf{x}_c$ (see Figure 3(b)).
- *Sac area* a_{sac}: area of the sac, which can be accurately computed if the surface representation is available.
- *Sac volume* v_{sac}: volume of the sac, which can be accurately computed if the surface representation is available.

These measurements are typically used by clinicians to select the treatment to follow and, additionally, they have been linked to aneurysm risk of rupture [3, 7]. The values of a_{sac} and v_{sac} cannot be manually computed from the image in an accurate manner. Thus, these

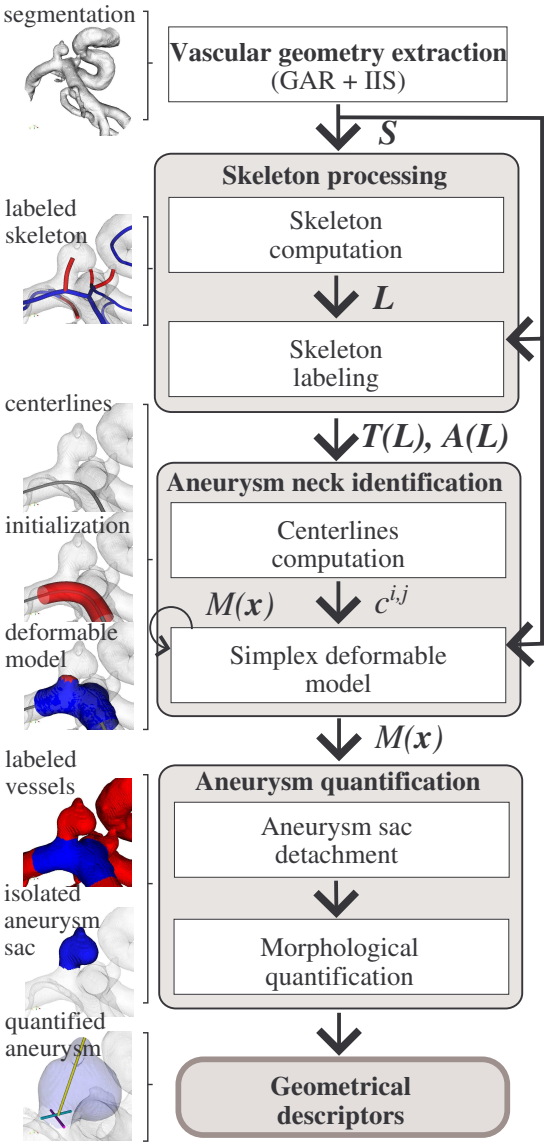

FIG. 2: Automated aneurysm morphological analysis and quantification steps. The proposed method goes from the vascular anatomy provided as a surface to the morphological analysis and quantification. The steps involved are skeleton processing, aneurysm neck identification and aneurysm quantification.

two measurements were only computed for the surface representations extracted from the segmentation.

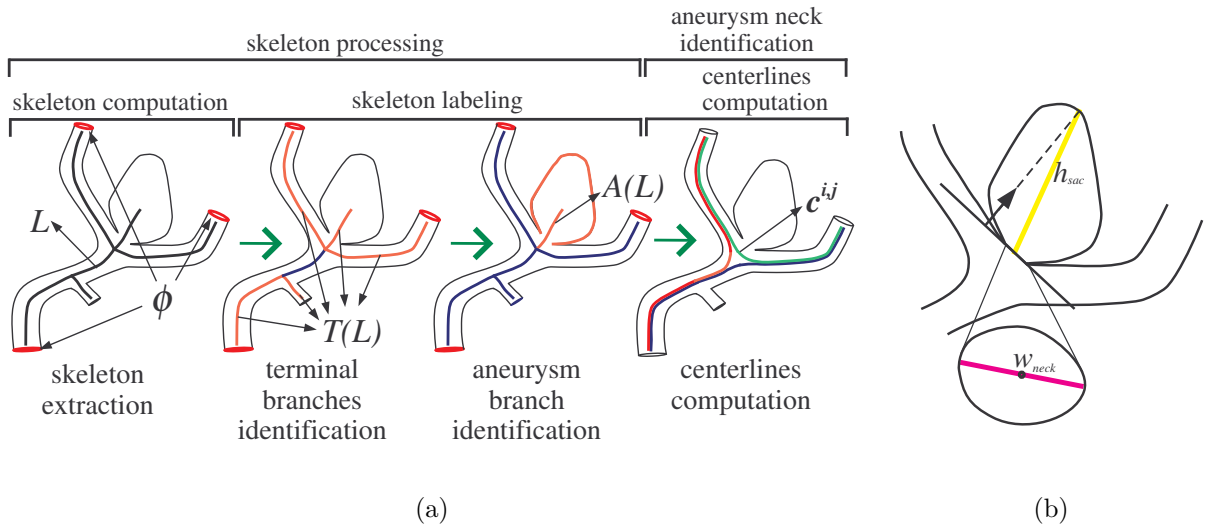

(a) (b)

FIG. 3: Detail of the skeleton labeling and centerline computation, which is part of the skeleton processing and aneurysm neck identification steps. (a) During the analysis of the skeleton L, the terminal branches $T(L)$ (connected on one end to the rest of L) are identified. By analyzing the proximity of these branches to the geometry boundaries ($\phi \subset C(S)$), possible aneurysm branches are detected. In the last step are presented the centerlines $c^{i,j}$ computed from L. (b) Measurements obtained from the automatic aneurysm quantification: neck width w_{neck} (magenta) and sac height h_{sac} (in yellow).

III. EXPERIMENTS AND RESULTS

The proposed methodology allows automatically isolating the aneurysm sac from a segmentation of the vascular ROI and quantifying their morphology by extracting anatomical measurements. This method's performance and accuracy was assessed by comparing its results with their equivalent manually extracted measurements.

A set of twenty-six (n=26) saccular intracranial aneurysm geometries collected during the European project @neurIST [25] have been used for the assessment of the proposed methodology. These have been obtained from diagnostic 3D rotational angiographic (3DRA) images, which have been acquired using either an Integris^{TM} Allura System (Philips Healthcare, Best, The Netherlands) or an AXIOM Artis (Siemens Medical Solutions, Erlangen, Germany). Voxel pitch in the reconstructed 3D images ranged from 0.208 mm to 0.378 mm and the image sizes were 256^3 or 512^3 voxels with 16 bits of depth per voxel. The aneurysm sac morphology was measured and compared for all the cases using the three

methods described below:

Manual Measurements by Clinicians (MMC): three independent clinical observers (neuroradiologists, with more than 10 years of experience) have measured the two variables directly on the image as they normally do in their daily clinical practice. The images were visualized using volume rendering and the measurements were obtained using a three dimensional measuring tool. The software AngioLab [26] was used for this purpose.

Automated measurements after Manual Sac Isolation (MSI): First, to generate the surface representation of the vascular wall, the method GAR described in Section II A was used. The neck was manually delineated for each aneurysm and the sac was isolated from the vascular wall surface representation by three independent observers experts in vascular image analysis, using the software AngioLab [26]. For this task, a series of points delimiting the neck of the aneurysm were selected over the generated surface. The criteria followed by the observers to isolate each aneurysm were

- the aneurysm separates from the parent vessel at its neck and
- the aneurysm has only one opening.

Measurements obtained using this method were considered the gold standard as they were computed in 3D (i.e., independently from the view point) and were isolated by experts in vascular image analysis. The average between the three observations was considered as the true value for each measurement.

Automated measurements after Automated Sac Isolation (ASI): Once the vascular geometry was extracted with GAR method (Section II A) and a surface representation of the vascular wall was obtained, the methodology proposed in this paper was used to isolate and quantify the aneurysm sac.

Additionally, a_{sac} and v_{sac} were automatically computed for MSI and ASI. All sacs were quantified following the same procedure described in Section II D.

A. Accuracy experiments on synthetic phantom

To assess which of the three methods, namely MMC, MSI or ASI, is the most accurate, one experiment was performed where a digital phantom of known shape and size was inserted in a 3DRA image. This digital phantom, which has a resolution of 0.02mm (ten times more

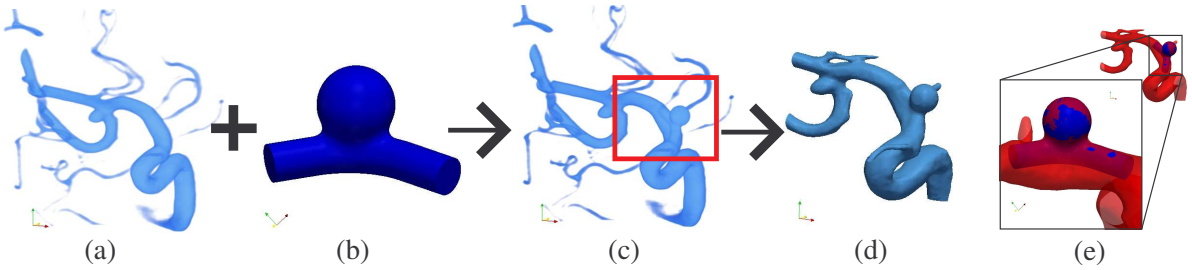

FIG. 4: Synthetic phantom embedded into a real 3DRA image. Intensities inside the phantom and its transition to the background were matched to those observed between the vessel and the background. (a) Original Image, (b) inserted phantom, (c) resulting image, (d) segmented mesh and (e) comparison between the original phantom and the segmented mesh.

than the image), was embedded it the image by registering in over the Internal Carotid Artery (Figure 4). The intensities inside the phantom are the same as the intensities inside the vessel and the transition between the interior of the phantom and the background was set to be the same (in intensity and length) as the transition between the vessel and the background. The resulting image was segmented using GAR. The aneurysm was quantified using the three methods (MMC on the image, MSI and ASI on the segmentation output). The ground truth measurements (w_{neck} and h_{sac}) were performed on the manually isolated dome from the original phantom high resolution surface and averaged through 3 manual isolations.

From these results presented in Table I, we observe that MSI method presents the lower error with respect to the ground truth (MMC = 6.06%, MSI = 4.07% and ASI = 7.67% for w_{neck} and MMC = 5.63%, MSI = 3.53% and ASI = 5.49% for h_{sac}). Also, the inter-observer variability appears to be larger for MMC method (above 4.5% for MMC, compared to 2% for MSI and 0% for ASI).

B. Results on real data

Figure 5 illustrates the results obtained with the three methods for ten aneurysms. Measurements corresponding to the observer with the largest difference with respect to the ASI, are shown.

Table II summarizes the measurements obtained by the three methods on the population

TABLE I: Assessment of the three quantification methods. Measurements are presented in mm in the first row (inter observer variability in parenthesis) and the error with respect to ground truth measurements as percentage (e_{GT}) is presented in the second row.

	Ground truth	MMC	MSI	ASI
w_{neck}	3.52 (1.28%)	3.31 (5.1%)	3.66 (2.02%)	3.79 (0%)
e_{GT}	0%	6.06%	4.07%	7.67%
h_{sac}	3.58 (0.97%)	3.68 (4.5%)	3.71 (1.70%)	3.78 (0%)
e_{GT}	0%	5.63%	3.53%	5.49%

TABLE II: Mean and standard deviation for the measurements obtained from the three methods indicated as μ (σ)

	w_{neck} (mm)	h_{sac} (mm)	a_{sac} (mm^2)	v_{sac} (cm^3)
MMC	3.36 (1.06)	5.53 (2.07)	-	-
MSI	4.31 (1.16)	5.81 (2.48)	101.8 (74.1)	0.111 (0.109)
ASI	4.29 (1.42)	5.51 (2.56)	95.79 (71.1)	0.104(0.102)

considered. For MMC and MSI, the measurements by the three observers were averaged and the mean (μ) and standard deviation (σ) were computed. For ASI, a unique measurement exists for each dimension of the aneurysm. We observe that mean values and standard deviations are more similar between MSI and ASI than with respect to MMC.

1. Repeatability

In Table III we report the standard deviation (σ) between observers for MMC and MSI methods. This coefficient indicates the maximum difference that is likely to occur between two measurements by the same method. We observe that the inter-observer variability of MMC is larger than that of MSI in all the measurements. For ASI, there is no inter-observer variability.

TABLE III: Inter-observer repeatability. Standard deviation

	w_{neck} (mm)	h_{sac} (mm)	a_{sac} (mm^2)	v_{sac} (cm^3)
MMC	0.47	0.75	-	-
MSI	0.17	0.12	2.44	0.00357

TABLE IV: Results for paired two sample t-test for equal means (two tailed p-vales) between the different methods. The p-values for each variable are reported.

Two sample paired t-test for means (two tailed p-values)

w_{neck}/h_{sac}		
MMC *vs.* MSI	**MMC *vs.* ASI**	**MSI *vs.* ASI**
p <0.001/p =0.002	p <0.001/p =0.95	p =0.43/p =0.95

2. Agreement

Assuming that the aneurysm measurements present a normal distribution, a paired two sample t-test, with the null hypothesis that differences between the two measurement methods is zero, was performed pair-wise between the observations for the three methods. Each method was compared to the other two for each variable (results are summarized in Table IV). It was found statistical significance to believe that the difference between MMC and MSI is not zero for both measurements, thus rejecting the null hypothesis. For the comparison between MMC and ASI, the measurements corresponding to neck width, the null hypothesis was also rejected. On the contrary, the differences between the sac measurements were not significant (p=0.95). The comparison between MSI and ASI, revealed no evidence for them to be different, thus requiring further analysis. From the results presented in section III A, we state that MSI method is more arateTo the best of our knowledge, this happened because the MMC method is fully manual and performed on the image, thus depending on the observer's point of view and visual criteria for performing each measurement. On the other hand, MSI and ASI are based on the quantification of a surface (either manually or automatically isolated), making the criteria identical in all cases.

Bland-Altman analysis [27] was used to assess the agreement between MSI and ASI further. As the surface representation of the aneurysm sac was available, other two morphological measurements, namely aneurysm sac area (a_{sac}) and volume (v_{sac}) were included.

TABLE V: Agreement between MSI and ASI

Bias (SE) and upper and lower LoA between MSI and ASI

	w_{neck}	h_{sac}	a_{sac} (mm^2)	v_{sac} (cm^3)
bias (SE)	-0.11 (0.12)	-0.16 (0.09)	-6.05 (1.32)	-0.0068 (0.002)
upper/lower LoA	1.26/-1.48	0.83/-1.16	8.17/-20.27	0.022/-0.036

These measurements could not be accurately computed directly on the image (e.g., using MMC). Results are summarized in Table V. We presented the bias and the standard error (SE) of the sample mean. Also, the upper and lower 95% Limits of Agreement (LoA $= \mu + 2\sigma / \mu - 2\sigma$) are shown. Figure 6 presents the Bland-Altman plots comparing MSI and ASI and presenting all the individual measurements together. The results for w_{neck} (Figure 6(a)), h_{sac} (Figure 6(b)), a_{sac} (Figure 6(c)) and v_{sac} (Figure 6(d)), are presented. A black solid line represents the bias and two dashed gray lines show the upper and lower LoA. We observe acceptable agreement between both methods, and the LoA were between 1 and 1.5 mm.

3. Efficiency

All the experiments were performed in an Intel Centrino 2 (2Gb of memory) with a NVidia GeForce 9300GS (512 Mb of memory) graphics card used for the acceleration of the volume rendering visualization. For the MMC, the medical images were automatically loaded by the software and presented to the clinician to perform the measurements. On average, 2min 51sec were required to perform the three measurements for each case. For MSI and ASI, the segmentation and the skeleton of the vascular anatomy were pre-computed. The GAR execution time depends on the size of the image and the size of the evolving surface, i.e., the amount of vasculature being segmented. On average, for a 256^3 voxels ROI, the execution time was 17±4 min (mean ± standard deviation) on a standard personal computer with an Intel quad-core 2.4GHz processor and 4GB of memory. The execution time is approximately linear on the size of the image, leading to execution times of less than a minute after the selection of a ROI around the aneurysm. The extraction of the skeleton took 20 seconds on average. These algorithms are not optimized and a more efficient implementation would certainly provide better execution times. The MSI sac extraction was done directly

on the segmentation output, which was manually loaded by the user. Considering the pre-processing (segmentation and skeletonization), manual isolation of one case took on average 2min 21 sec. The time needed for the automated isolation, including segmentation and skeletonization, was 2min 38sec on average. Finally, ASI method is suitable for parallelization, which would considerably reduce its computational time consumption, no parallelization or optimization were introduced in the implementation described in this work.

IV. DISCUSSION

In this paper, we presented a method for the automated isolation of intracranial aneurysm sac and its quantification. This method is based on the analysis of the vascular geometry skeleton, for the classification of vascular branches; and on deformable models, for the isolation of the aneurysm sac. Typical morphological measurements, such as aneurysm neck width, sac height, surface and volume, are automatically computed for the automatically isolated aneurysm.

Measurements obtained with the proposed methodology have been compared to measurements obtained by two manual methods. The first, MMC, consisted in the direct measurement on the images by experienced clinicians. The second, MSI, consisted in the manual neck delineation and isolation of the sac from the vascular surface representation by three experts in vascular image quantification. Automatically computed morphological measurements were obtained from the resulting sacs. To assess which of the three methods (i.e., MMC, MSI and ASI) is more accurate against the ground truth, a synthetic phantom presenting the features of a real image was generated. From this experiment, we observe that MSI method is performing the best in terms of accuracy. To the best of our knowledge, although this method does not completely remove inter-observer variability, it provides the most accurate measurement.

In accordance to this, measurements manually performed on the image by clinicians were found to be different from those performed automatically. We observed that the measurements performed on the images by the clinicians were different ($p < 0.005$) to the equivalent measurements on the surface. We attribute these differences to the fact that the image might bias one or more observers to use a particular viewing angle that is sub-optimal for that measurement. From our interpretation of the results, although the clinicians' measure-

ments were performed in three dimensions, in many situations the measurement is affected by the viewing angle (due to the shape of the aneurysm, its location or the presence of other vessels/image artifacts near the selected location, etc.) leading to inaccurate measurements. Furthermore, the MMC method, which is performed directly on the volume rendering, depends on the selection of the cut-off threshold used for rendering the image. In the authors opinion, the limitation of measuring directly on the images (MMC) that is eliminated when combining a robust segmentation and a manual or automatic (respectively for MSI and ASI) neck delineation tool and explains the larger variability of MMC. Only when comparing the sac height measured by MMC and ASI, no statistical significance was observed to conclude that these were different. Owing to the high statistical evidence indicating that clinicians' measurements and the automated ones are different, only MSI and ASI measurements were compared to each other.

We also noticed that the inter-observer variability for the MMC measurements was larger than that for MSI. For the MSI method a low variability was observed (σ=0.17mm and σ=0.12mm for neck width and sac height, respectively). We attribute this to the fact that MSI is more robust due to the simple criteria required for the isolation for the aneurysm. This, and the fact that the measurements are computed automatically on the surface, not requiring the selection of one particular view angle, makes these measurements more robust. For the ASI method, repeatability is guaranteed as it is automated.

Based on the agreement comparison results, we interpret that the proposed method is a good alternative for automated aneurysm sac isolation and quantification. For the neck width and the sac height, the bias (SE) of ASI with respect to MSI was found to be -0.11mm (0.12mm) and -0.16mm (0.09mm), which is approximately the image resolution. The slightly larger errors observed are on the w_{neck} because it is directly related to the neck definition than the h_{sac}, which is related to it but indirectly. Furthermore, near the neck the aneurysm shape is more irregular. These irregularities cause that small changes in the location of the neck (up or down) might have a larger impact on the w_{neck} than on the h_{sac}. Also, acceptable agreement was observed between both methods for a_{sac} and v_{sac} as can be clearly observed in the corresponding Bland-Altman plots.

The three methods required similar time to obtain the measurements. A more efficient implementation (e.g. using parallelization) would result in a considerable gain in the computational time of ASI providing a fast way to quantify an aneurysm without the need of

interaction by a human operator.

This method is a first approach towards the automated isolation of the aneurysm sac that was assessed using manually obtained measurements. Perhaps the most relevant advantage of this method is that it eliminates inter-observer variability.

The work previously developed by Ford et al. [14] proposed a method for aneurysm removal. In their work the authors identified the non-planar boundary (a 3D curve) separating the vessel and the aneurysm sac. Additionally, in the present work a method for determining a neck plane, which is essential for different morphological features of interest to the clinician, is proposed.

Looking from a broader point of view, this method could have a larger impact on the clinical practice by providing a unified criteria for treatment selection (coil, stent, etc.) based on simple aneurysm dimensions [3]. Nowadays, these practices are based on shared knowledge and experience, which is passed from clinician to clinician. Also, on the field of computational hemodynamics that is devoted to the study of intracranial aneurysms, this method could provide an observer independent way to determine the aneurysm neck [28, 29].

As a limitation, we could mention the performance of the methods in more complex aneurysm geometries. In principle, the method was designed for saccular aneurysms and not for multilobular or fusiform ones. For this kind of aneurysms there is no definition of the sac and the delineation of the original vessel is often subjective and questionable even for an expert.

V. CONCLUSIONS

In this paper, is proposed a methodology for automatically isolating the sac of intracranial aneurysms and computing morphological measurements. This methodology is based on skeleton topology analysis, for the classification of vessels in the vascular region of interest; and deformable models, for the detection of aneurysm ostium and isolation of the aneurysm sac. After this, the aneurysm morphological measurements (w_{neck} and h_{sac}) were calculated automatically. This method was evaluated on twenty-six intracranial aneurysm geometries. The results were compared with manual measurements performed by clinicians and automated measurements performed on manually isolated aneurysms by three independent observers. The quantitative assessment showed poor agreement between clinicians'

measurements and automated measurements. This limitation is due to the selection of sub-optimal view angle for the particular measurement. On the other hand, the automated measurement from isolated aneurysm are independent of the viewing angle as they are measured by a computer algorithm directly on the surface representation of the aneurysm sac, eliminating any bias or difference in criteria. The visual assessment of the automated isolation showed a good match between manual and automated isolations. Furthermore, the qualitative assessment of the results showed acceptable agreement between both methods.

Acknowledgments

The authors would like to thank Luigi Carotenuto and Valeria Barbarito for the support on the development of the manual quantification tools, David Capdeferro and Carolina Valencia for the organization and preparation of the image data and Chong Zhang for the generation of the digital phantom image. This work was partially supported within the CENIT-CDTEAM and CENIT-cvREMOD projects funded by the Spanish Ministry of Innovation and Science-CDTI and partly within the framework of the @neurIST Project (IST-2005-027703), which is co-financed by the European Commission within the IST Program of the Sixth Framework Programm.

---

[1] D. Wiebers and The International Study of Unruptured Intracranial Aneurysms Investigators, "Unruptured intracranial aneurysms: natural history, clinical outcome, and risks of surgical and endovascular treatment," Lancet **362**, 103–110 (July 2003).

[2] F. B. Meyer, J. H. III, and S. Riederer, "Pulsatile increases in aneurysm size determined by cine phase-contrast MR angiography," J. Neurosurg. **78**, 879–883 (1993).

[3] H. Ujiie, H. Tachibana, O. Hiramatsu, A. L. Hazel, T. Matsumoto, Y. Ogasawara, H. Nakajima, T. Hori, K. Takakura, and F. Kajiya, "Effects of size and shape (aspect ratio) on the hemodynamics of saccular aneurysms: A possible index for surgical treatment of intracranial aneurysms," Neurosurgery **45**, 119–130 (1999).

[4] W. C. K. Wong and A. C. S. Chung, "Augmented vessels for quantitative analysis of vascular abnormalities and endovascular treatment planning," IEEE Trans. Med. Imaging **25**, 665–684 (2006).

[5] X. Mellado, I. Larrabide, M. Hernandez, and A. F. Frangi, "Flux driven medial curve extraction," The Insight Journal **Jul-Dec, 2007**, http://hdl.handle.net/1926/560 (2007).

[6] B. Ma, R. E. Harbaugh, and M. L. Raghavan, "Three-dimensional geometrical characterization of cerebral aneurysms," Ann. Biomed. Eng. **32**, 264–273 (2004).

[7] M. L. Raghavan, B. Ma, and R. E. Harbaugh, "Quantified aneurysm shape and aneurysm rupture," Neurosurgery **102**, 355–362 (2005).

[8] S. Rohde, K. Lahmann, J. Beck, R. N. B. Y. A. Raabe, and J. Berkefeld, "Fourier analysis of intracranial aneurysms: towards an objective and quantitative evaluation of the shape of aneurysms," Neuroradiology **47**, 121–126 (2005).

[9] M. Kangasniemi, T. Mäkelä, S. Koskinen, M. Porras, and K. P. J. Hernesniemi, "Detection of intracranial aneurysms with two-dimensional and three-dimensional multislice helical computed tomographic angiography," Neurosurgery **54**, 336–341 (2004).

[10] H. Arimura, Q. Li, Y. Korogi, T. Hirai, H. Abe, Y. Yamashita, S. Katsuragawa, R. Ikeda, and K. Doi, "Automated computerized scheme for detection of unruptured intracranial aneurysms in three-dimensional magnetic resonance angiography," Acad. Radiol. **11**, 1093–104 (2004).

[11] H. Arimura, Q. Li, Y. Korogi, T. Hirai, S. Katsuragawa, Y. Yamashita, K. Tsuchiya, and K. Doi, "Computerized detection of intracranial aneurysms for three-dimensional mr angiography: Feature extraction of small protrusions based on a shape-based difference image technique," Med. Phys. **33**, 394–401 (2005).

[12] A. D. Fleming, S. Philip, K. A. Goatman, J. A. Olson, and P. F. Sharp, "Automated microaneurysm detection using local contrast normalization and local vessel detection," IEEE Trans. Med. Imaging **25**, 1223–1232 (2006).

[13] Y. Uchiyama, H. Ando, R. Yokoyama, T. Hara, H. Fujita, and T. Iwama, "Computer-aided diagnosis scheme for detection of unruptured intracranial aneurysms in mr angiography," Proceedings of the 2005 IEEE Engineering in Medicine and Biology 27th Annual Conference Shanghai, China, September 1-4, 2005 3031–3034 (2005).

[14] M. D. Ford, Y. Hoi, M. Piccinelli, L. Antiga, and D. A. Steinman, "An objective approach to digital removal of saccular aneurysms: technique and applications," Br. J. Radiol. **82**, S55–S61 (2009).

[15] M. Piccinelli, A. Veneziani, D. A. Steinman, A. Remuzzi, and L. Antiga, "A framework for geometric analysis of vascular structures: Application to cerebral aneurysms," IEEE Trans.

Med. Imaging **28**, 1141–1155 (2009).

[16] A. Lauric, E. Miller, S. Frisken, and A. M. Malek, "Automated detection of intracranial aneurysms based on parent vessel 3D analysis," Med. Image Anal. **14**, 149–159 (2010).

[17] W. van Rooij, M. Sprengers, A. de Gast, J. Peluso, and M. Sluzewski, "3D rotational angiography: The new gold standard in the detection of additional intracranial aneurysms," Am. J. Neuroradiol. **29**, 976–979 (2008).

[18] M. Hernandez and A. F. Frangi, "Non-parametric geodesic active regions: Method and evaluation for cerebral aneurysms segmentation in 3DRA and CTA," Med. Image Anal. **11**, 224–241 (2007).

[19] H. Bogunovic, J. M. Pozo, M.-C. Villa-Uriol, C. B. L. M. Majoie, R. v. d. Berg, H. A. F. G. van Andel, J. M. Macho, J. Blasco, L. S. Romn, and A. F. Frangi, "Automated segmentation of cerebral vasculature with aneurysms in 3dra and tof-mra using geodesic active regions: An evaluation study," Med. Phys. **38**, doi:10.1118/1.3515749 (2011).

[20] S. Bouix, K. Siddiqi, and A. Tannenbaum, "Flux driven automatic centerline extraction," Medical Image Analysis **9**, 209–221 (2005).

[21] A. K. Jain, *Fundamentals of Digital Image Processing* (Prentice Hall, 1989).

[22] J. Montagnat and H. Delingette, "4D deformable models with temporal constraints: application to 4D cardiac image segmentation," Med. Image Anal. **9**, 87–100 (2005).

[23] J. Montagnat and H. Delingette, "Globally constrained deformable models for 3D object reconstruction," Signal Process. **71**, 173–186 (December 1998).

[24] H. Delingette, "General object reconstruction based on simplex meshes," Int. J. Comput. Vis. **32**, 111–142 (1999).

[25] A. F. Frangi, D. R. Hose, and D. A. Ruefenacht, "The @neurIST project: Towards understanding cerebral aneurysms." SPIE Newsroom, (2007).

[26] M. C. Villa-Uriol, I. Larrabide, A. J. Geers, J. Pozo, H. Bogunovic, P. Omedas, V. Barbarito, L. Carotenuto, C. Riccobene, X. Planes, Y. Martelli, and A. Frangi, "Angiolab: Integrated technology for patient-specific management of intracranial aneurysms," Proceedings of the IEEE Engineering in Medicine and Biology Conference 2010, Buenos Aires, Argetina (2010).

[27] J. M. Bland and D. G. Altman, "Statistical methods for assessing agreement between two methods of clinical measurement," The Lancet **327**, 307–310 (1986).

[28] A. G. Radaelli, L. Augsburger, J. R. Cebral, M. Ohta, D. A. Rüfenacht, R. Balossino, G. Ben-

ndorf, D. R. Hose, A. Marzo, R. Metcalfe, P. Mortier, F. Mut, P. Reymond, L. Socci, B. Verheghe, and A. F. Frangi, "Reproducibility of haemodynamical simulations in a subject-specific stented aneurysm model - a report on the virtual intracranial stenting challenge 2007," J. Biomech. **41**, 2069–2081 (2008).

[29] I. Larrabide, M. Kim, L. Augsburger, M. C. Villa-Uriol, D.Rüfenacht, and A. F. Frangi, "Fast virtual deployment of self-expandable stents: method and in-vitro evaluation for intracranial aneurysmal stenting," Med. Image Anal. **DOI: http://dx.doi.org/10.1016/j.media.2010.04.009** (2010).

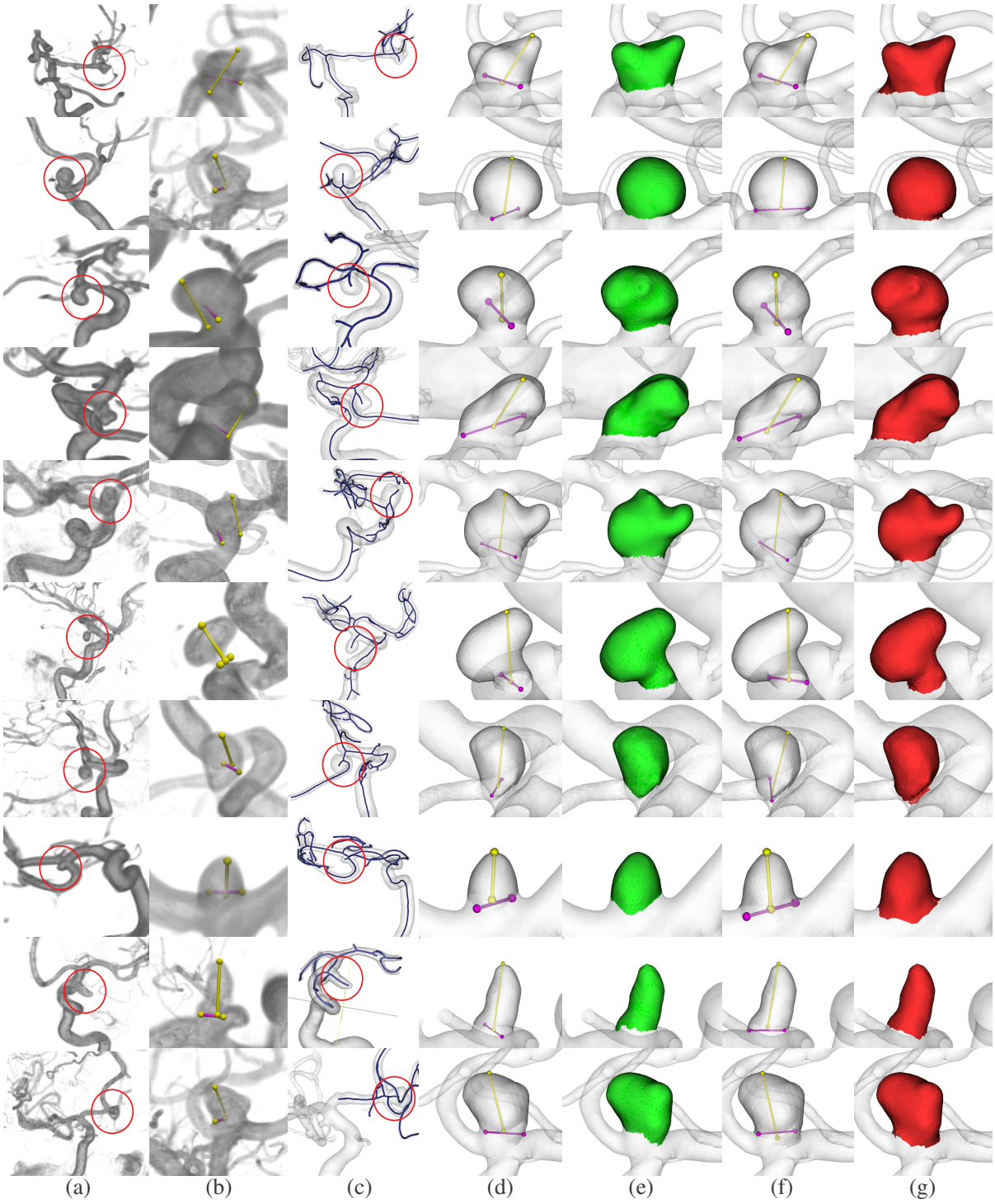

FIG. 5: Intermediate steps and results for 10 vessel geometries with aneurysms obtained from 3DRA images. From left to right, the different columns present (a) volume rendering of the 3DRA image, (b) measurements performed by the clinician, (c) segmented models and their skeleton, (d) automatically computed measurements and (e) corresponding automatically isolated sac (green), (f) automatically computed measurements and (g) corresponding manually isolated sac (red).

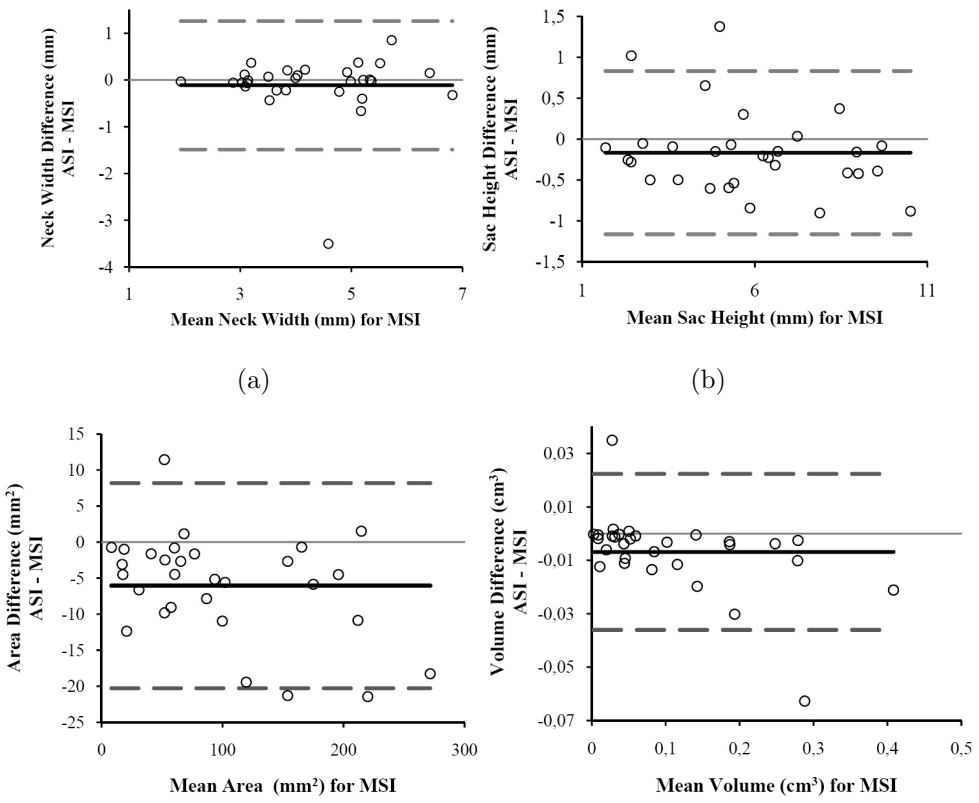

FIG. 6: Bland-Altman plots comparing the results for MDI and ADI. ADI was compared to the mean of the three observations by MDI. The plots compare the neck width (a), sac height (b), area (c) and volume (d). The black solid line represents the bias and the dashed gray lines the upper and lower 95% LoA.